remote sensing

MDPI

Article

Gravity Predictions in Data-Missing Areas Using Machine Learning Methods

Yubin Liu [1], Yi Zhang [1,*], Qipei Pang [2], Sulan Liu [2], Shaobo Li [2], Xuguo Shi [2], Shaofeng Bian [1,2] and Yunlong Wu [2]

[1] Key Laboratory of Geological Survey and Evaluation of Ministry of Education, China University of Geosciences, Wuhan 430074, China; liuyb@cug.edu.cn (Y.L.); bianshaofeng@cug.edu.cn (S.B.)
[2] School of Geography and Information Engineering, China University of Geosciences, Wuhan 430074, China; pqp0111@cug.edu.cn (Q.P.); sulanliu@cug.edu.cn (S.L.); lishaobo@cug.edu.cn (S.L.); shixg@cug.edu.cn (X.S.); wuyunlong@cug.edu.cn (Y.W.)
* Correspondence: zhangyi11@cug.edu.cn

Abstract: Gravity data, comprising a key foundational dataset, are crucial for various research, including land subsidence monitoring, geological exploration, and navigational positioning. However, the collection of gravity data in specific regions is difficult because of environmental, technical, and economic constraints, resulting in a non-uniform distribution of the observational data. Traditionally, interpolation methods such as Kriging have been widely used to deal with data gaps; however, their predictive accuracy in regions with sparse data still needs improvement. In recent years, the rapid development of artificial intelligence has opened up a new opportunity for data prediction. In this study, utilizing the EGM2008 satellite gravity model, we conducted a comprehensive analysis of three machine learning algorithms—random forest, support vector machine, and recurrent neural network—and compared their performances against the traditional Kriging interpolation method. The results indicate that machine learning methods exhibit a marked advantage in gravity data prediction, significantly enhancing the predictive accuracy.

Keywords: gravity data prediction; machine learning; random forest; recurrent neural network; support vector machine

check for updates

Citation: Liu, Y.; Zhang, Y.; Pang, Q.; Liu, S.; Li, S.; Shi, X.; Bian, S.; Wu, Y. Gravity Predictions in Data-Missing Areas Using Machine Learning Methods. *Remote Sens.* **2024**, *16*, 4173. https://doi.org/10.3390/rs16224173

Academic Editors: Giuseppe Casula, Conrad M. Albrecht, Martin Werner, Levente Klein and Salman Khan

Received: 25 August 2024
Revised: 17 October 2024
Accepted: 6 November 2024
Published: 8 November 2024

Copyright: © 2024 by the authors. Licensee MDPI, Basel, Switzerland. This article is an open access article distributed under the terms and conditions of the Creative Commons Attribution (CC BY) license (https://creativecommons.org/licenses/by/4.0/).

1. Introduction

Land subsidence, characterized by the sinking of the Earth's surface, can be attributed to material distribution changes in geological structures. It is possible to ascertain the rate and extent of subsidence by monitoring the variations in gravity anomalies within the affected area [1–6]. Generally, tasks of land subsidence monitoring typically require highly precise gravity measurement data [7,8]. However, gravity surveys are challenging to conduct in certain regions because of environmental and technological constraints, particularly within remote mountainous and lacustrine areas. The difficulty in data collection in these regions results in considerable data gaps, thereby generating measurement blank areas [9,10]. Acquiring gravity data from measurement blank areas remains a challenge; consequently, suitable predictive methods are essential for inferring the gravity data in these unknown regions [11].

Traditional gravity data prediction relies mainly on interpolation methods, including distance-weighted inverse interpolation [12], spline interpolation [13], improved Shepard interpolation [14], radial basis function interpolation [15,16], and Kriging interpolation [17–19]. The distance-weighted inverse interpolation method is computationally straightforward and efficient, utilizing the spatial coordinates of known sample points to estimate values at unsampled locations. This estimation employs the inverse distances between known sample points and the estimation targets as weighting factors [12]; the spline interpolation method, known

for its adaptability and ease of use, effectively addresses the issue of data intervals by constructing continuous functions through piecewise polynomials, thereby facilitating subsequent modeling and analysis [13]; the Shepard interpolation method effectively integrates global and local interpolation features [20], with its enhancements aimed at reducing the effects of outliers and improving data smoothness; the radial basis function interpolation method is suitable for high-dimensional data. Constructed using Euclidean distance, the weighted sum of these basis functions is used to form the interpolation function. Kriging interpolation, a widely used method, estimates the value at an unsampled point by computing the weighted average of surrounding data points, thereby effectively minimizing inversion uncertainty and enhancing the resolution [17,21]. Each of the interpolation methods mentioned above possesses unique advantages; however, their accuracy varies, particularly in regions of sparse gravity data. The existing methods may not consistently satisfy the accuracy requirement, potentially leading to significant predictive errors [22].

The rapid development of artificial intelligence has demonstrated the substantial potential of machine learning algorithms [23,24]. Machine learning algorithms, when applied to data analysis, enhance both the efficiency of data processing and the precision of predictive outcomes [25,26], thereby ensuring more reliable results. Machine learning technology has been extensively applied across various fields, promoting industrial development [27], and some methods, including random forest (RF), support vector machine (SVM), and neural networks, are gaining increasing attention in geophysics and are being effectively implemented [28–34]. A new spatial interpolation method called random forest spatial interpolation (RFSI), based on the random forest method, was introduced, offering significant computational efficiency [35]. Certain studies have introduced a real-time forecasting approach—Recurrent Neural Network-Recursively Updated Forecasting (RNN-RUF)—which is predicated on recurrent neural networks (RNNs) to dynamically predict the production of shale gas wells. The RUF framework takes the structure of time series data into account, avoiding sequence segmentation, thereby improving training efficiency and exhibiting superior performance [36]. The SVM algorithm has been widely applied in flood prediction. A hybrid model integrating the SVM with the Gray Wolf Optimizer (GWO) has shown superior predictive performance, better than Multilayer Perceptron (MLP), during both the training and testing stages [37].

This study aims to evaluate the potential of machine learning methods in the field of gravity data prediction. For this purpose, three algorithms, including RF, SVM, and RNN, are selected for analysis to verify their prediction performance. Based on the EGM2008 satellite gravity model, this study conducts simulations on datasets of different sizes and comprehensively compares them with the traditional Kriging interpolation method, thereby analyzing the accuracy differences in gravity data predictions among various algorithms.

2. Methods

2.1. Recurrent Neural Network (RNN)

An RNN is a neural network structure suitable for dealing with sequence data [38]. The core of its design is to introduce recurrent connections in the network to give the network memory capabilities and to learn vector-to-vector mappings through internal self-connections [39] to capture dynamic behavior and long-term dependencies in time series.

Within the RNN model, the state of the hidden layer at the current time step is influenced not only by the current input but also by the output of the hidden layer from the preceding time step because of the recurrent connections. The relationship between input and output satisfies Equations (1) and (2), where tanh and softmax are both activation functions [40,41].

$$s_t = \tanh(Ux_t + Ws_{t-1} + \mathrm{b}_s) \quad (1)$$

$$o_t = \mathrm{softmax}(V_t s_t + \mathrm{b}_o) \quad (2)$$

2.2. Random Forest (RF)

The RF is a bagging model of decision trees; it improves model accuracy and robustness by constructing multiple decision trees and employs random attribute selection during the training process of these trees [42].

The core of the RF algorithm is to construct a single decision tree by randomly selecting subsets of features and samples. Through multiple iterations, a random forest model is formed based on the generation of multiple independent decision trees. The final prediction result is determined by a majority voting mechanism to improve the accuracy of the model [43,44].

The equation of the decision tree is as follows:

$$L = \min_{j,s}\left[\min_{d_1}\sum_{x_i \in m_1(j,s)}(y_i - d_1)^2 + \min_{d_2}\sum_{x_i \in m_2(j,s)}(y_i - d_2)^2\right] \tag{3}$$

In the above Equation (3), m_1 and m_2 denote the input data, y_i represents the tag value, and d_1 and d_2 correspond to the average output values for each respective partitioning unit.

2.3. Support Vector Machine (SVM)

The fundamental principle of the SVM involves finding an optimal hyperplane within the feature space that serves as the decision boundary, distinguishing among different sample categories. This hyperplane maximizes the interval, defined as the distance from the nearest sample points to the hyperplane, thereby enabling the prediction of labels from one or more feature vectors [45–47]. Among the many kernel functions available for the SVM, the Gaussian Radial Basis Function (RBF) kernel is particularly favored for its broad applicability [48,49]. Consequently, the RBF kernel is chosen in this study to execute the necessary kernel operations.

In Equation (4), $K(x_i, x_j)$ is the kernel function; γ denotes the hyperparameter that controls the RBF kernel function; x_i and x_j are the feature vectors of the i-th and j-th samples, respectively. The expression of the Gaussian radial basis kernel can be found in the following equation:

$$K(x_i, x_j) = \exp\left(-\gamma\left|\left|x_i - x_j\right|\right|^2\right), \gamma > 0 \tag{4}$$

2.4. Kriging

Kriging, a spatial interpolation method, estimates values of unsampled regions by establishing a spatial correlation model among known data points. The Kriging method employs a semi-variogram function to quantify dependencies among spatial data points, characterizing the systematic variance changes as the distance between these points increases [18,50–52]. Within this method, variance and covariance, which represent the degree of variation and the spatial correlation between data points, respectively, are precisely estimated by minimizing the prediction error. Utilizing these estimated values, the Kriging method constructs a functional model, thereby enabling effective prediction of values in unsampled areas.

There are three functional models commonly utilized in spatial analysis: the spherical, exponential, and Gaussian models [45], and the Gaussian model in Equation (5) is selected in this study, where $\gamma(\mathrm{h})$ denotes the variation function, h represents the spatial distance, and C_0 is the parameter to be estimated.

$$\gamma(\mathrm{h}) = \begin{cases} 0, & \mathrm{h} = 0 \\ C_0 + C\left(1 - \mathrm{e}^{-\frac{\mathrm{h}^2}{\mathrm{a}^2}}\right), & \mathrm{h} > 0 \end{cases} \tag{5}$$

3. Simulation Experiments

3.1. Gravity Data

The spatially uniformly distributed gravity datasets used in simulation experiments are derived from the EGM2008 satellite model [53]. Given the strong correlation between gravity and topography, the study area was chosen for its diverse terrain, including both flat and complex landscapes. To assess the efficacy of the four methods utilized in gravity data prediction, the central-eastern region of China was selected in this study as the sampling area for a large-scale dataset. This region, as described in Figure 1, encompasses key areas of Hunan, Hubei, Henan, Anhui, and Jiangxi provinces. The large-scale dataset comprises a total of 46,080 gravity measurements and covers regions with varied terrain; the western and southeastern areas exhibit more undulating landscapes, whereas the central and northeastern areas are characterized by flatter terrain. In contrast, the small-scale dataset, as described in Figure 2, derived from a part of Henan province, is a dataset formed by selecting a small area within the large-scale dataset, featuring elevated terrain in the west and mainly flat terrain in the central and eastern regions, as well as a total of 1152 gravity measurements.

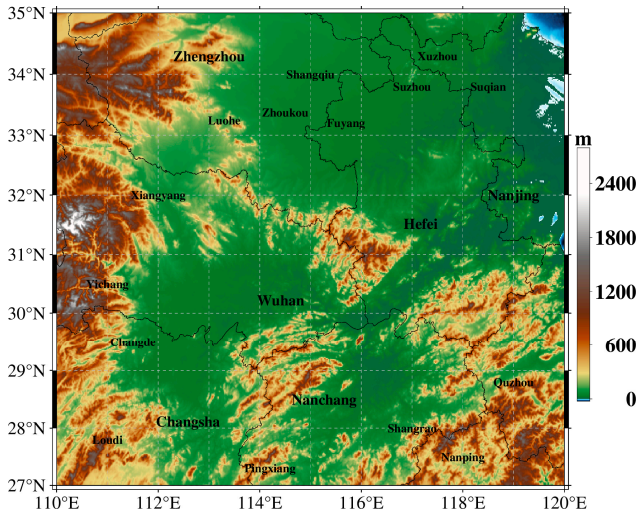


Figure 1. Terrain relief for large-scale dataset area.

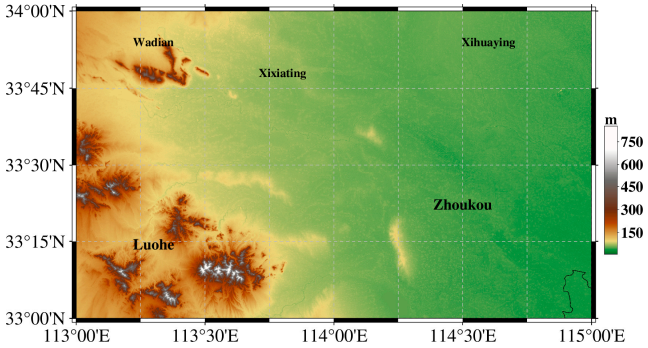


Figure 2. Terrain relief for small-scale dataset area.

3.2. Experiments Configuration

Figures 3 and 4 show the regional gravity anomalies for large- and small-scale datasets, respectively. In the large-scale dataset (Figure 3), high gravity values are mainly concentrated in the northeastern region, whereas the central and southwestern regions exhibit relatively lower values. Conversely, negative gravity anomaly values are primarily found in the western part of the study area. In the small-scale dataset (Figure 4), high gravity values are concentrated in the northwestern and southwestern regions, with the remaining areas mainly displaying negative values. An obviously negative correlation between gravity

anomalies and terrain relief across the study area can be revealed by the comparison of Figures 1 and 2 with Figures 3 and 4.

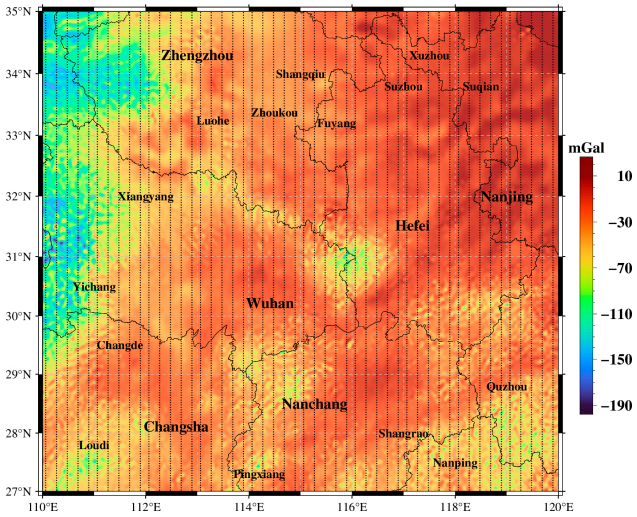


Figure 3. Fixed selection experiment configuration for the large-scale dataset (the black dots represent the data points of the testing set).

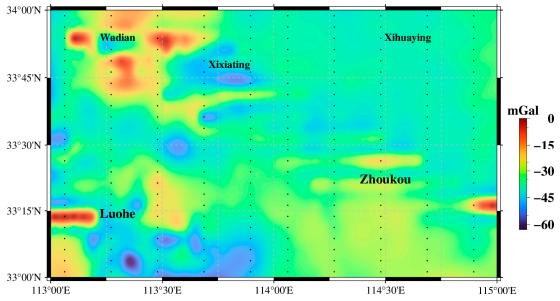


Figure 4. Fixed selection experiment configuration for the small-scale dataset (the black dots represent the data points of the testing set).

This study employs both fixed and random selection methods to construct the training and testing datasets. In the fixed selection experiment, for the large-scale dataset, given that there are 192 data points at the same longitudes, to preserve data integrity, 50 data points per longitude are sampled, totaling 9600 data points for the testing set across the entire region (as shown in Figure 3). The remaining 36,480 data points are used as the training set. Similarly, for the small-scale dataset, with 24 data points at the same longitudes, 5 data points per longitude are selected in this experiment. The entire area's testing set comprises 240 data points, as illustrated in Figure 4, while the remaining 912 data points form the training set.

The random selection experiment employs a 10-fold cross-validation to assess the four methods. The large-scale dataset contains a total of 46,080 data points, and the small-scale dataset includes 1152 data points. The models of the four methods are trained on both large- and small-scale training sets and subsequently utilized to predict the data.

Several metrics to evaluate the model's performance, including the mean absolute difference between predicted and observed values, standard deviation (SD) of these differences, mean absolute percentage error (MAPE), mean absolute error (MAE), root mean square error (RMSE), and the coefficient of determination R^2, where n is the number of samples, Z_i^{sim} and A_i represent the i-th predicted value, and Z_i^{obs} and F_i represent the i-th true value.

The equations for *MAPE* and *MAE* are presented as follows:

$$MAPE = \frac{100\%}{n}\sum_{i=1}^{n}\left|\frac{A_i - F_i}{A_i}\right| \tag{6}$$

$$MAE = \frac{1}{n}\sum_{i=1}^{n}\left|Z_i^{\text{sim}} - Z_i^{\text{obs}}\right| \tag{7}$$

The *RMSE* denotes the standard deviation of the residuals, measuring the deviation between the model's predictions and the true values, and a lower *RMSE* indicates superior predictive accuracy [54]. The equation for *RMSE* is provided below:

$$RMSE = \sqrt{\frac{1}{n}\sum_{i=1}^{n}\left(Z_i^{\text{sim}} - Z_i^{\text{obs}}\right)^2} \tag{8}$$

Table 1 lists the model configurations for the three machine learning algorithms.

Table 1. Model configuration.

Methods	Parameters	Values
RF	Number of decision trees	100
SVM	Kernel function	Radial basis function
RNN	RNN layer	3
	Number of hidden layer neurons	64
	Learning rate	0.02
	Num-epochs training times	2000
	Criterion	MSE
	Optimizer	Adam

3.3. Fixed Selection Experiment

Based on the gravity data from the testing set, predicted values can be derived from the RNN, RF, SVM, and Kriging methods. For the large-scale dataset, a subset of 50 data points is selected to plot in Figure 5. Among these, the 30th data point represents the minimum value and serves as a reference for assessing the predictive capabilities of each method. Meanwhile, the RF and RNN methods exhibit superior predictive performance of approximately 2.37 mGal and 12.45 mGal, respectively, with minimal difference between these predictions and the true values. In contrast, the SVM and Kriging methods yield predictions of 25.1 mGal and 22.31 mGal, respectively, demonstrating significant deviations from the true values across both datasets.

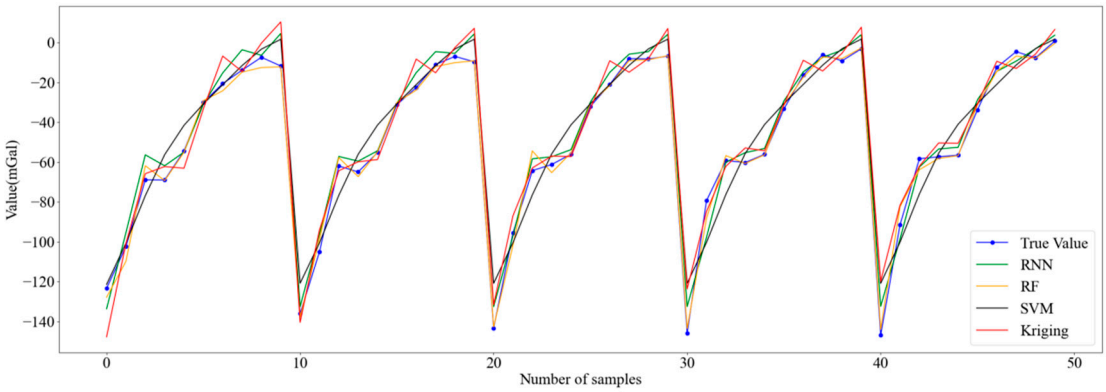


Figure 5. Predicted and true values of the four methods for the large-scale dataset. The blue curve is the true gravity value, and the green, orange, black, and red curves are predicted values for the RNN, RF, SVM, and Kriging methods, respectively. The horizontal axis is the number of samples, and the vertical axis is the predicted values.

For the small-scale dataset, the 50th data point displayed in Figure 6 was chosen for comparison. This point, exhibiting significant differences, can, to some extent, reflect the characteristics and complexity of the entire dataset, offering an assessment of the predictive performance of each method. The results indicate that the RF method's predicted value at this point differs from the true value by 2.08 mGal, with the predicted curve closely following the trend of the true value, indicating a superior prediction effect. The RNN method's prediction for this data point is slightly less, approximately 0.59 mGal, and more closely consistent with the true value's curve trend. In contrast, the SVM and Kriging methods' predicted values deviate significantly from the true value, with differences of approximately 24.96 mGal and 24.03 mGal, respectively, and do not fit well to the true value curve.

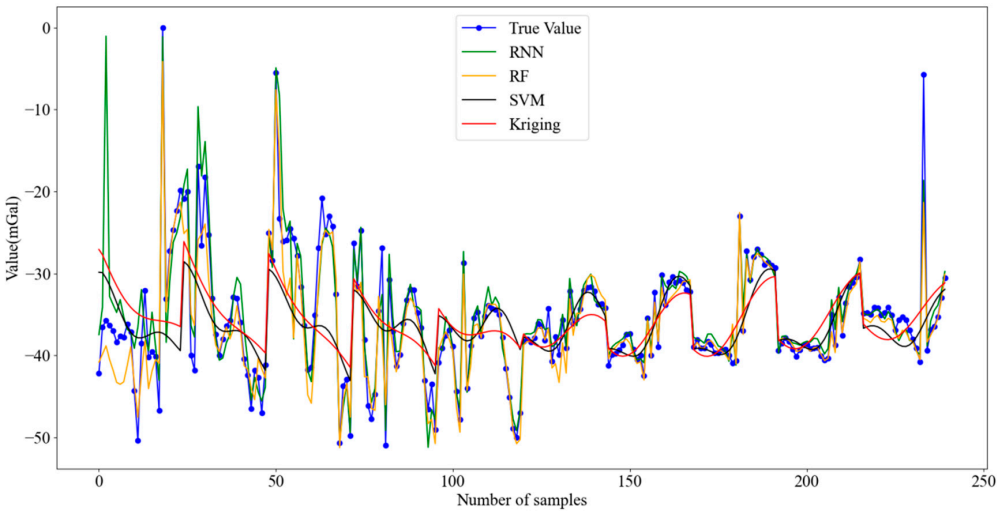


Figure 6. Predicted and true values of the four methods for the small-scale dataset. The blue curve is the true gravity value, and the green, orange, black, and red curves are predicted values for the RNN, RF, SVM, and Kriging methods, respectively. The horizontal axis is the number of samples, and the vertical axis is the predicted values.

Figures 7 and 8 show the predicted and original gravity data obtained from the four methods for both large- and small-scale datasets, respectively. The fixed selection experiment prediction data points are displayed as black dots in Figures 3 and 4, while the predicted values are represented by strip distributions in the figures. In the gravity data map, the difference between data points and their adjacent points becomes more obvious when there is a significant residual between predicted and true values, resulting in a streaking effect. Comparative analysis reveals that the differences between the predicted and original gravity values for the RF and RNN methods are minimal across both scales, indicating good predictive performance. In contrast, the SVM and Kriging methods exhibit an obvious streak effect and poor predictive performance on both large- and small-scale datasets.

Figure 9 illustrates the frequency distribution of differences (FDD) between the predicted and true values for the large-scale dataset. Analysis reveals that the RF method's differences mainly lie within the −10 to 10 range, with a higher concentration in this interval. Among the four methods, the RF method exhibits the highest FDD near zero, indicating its superior predictive performance for the large-scale dataset. The RNN method's predicted differences are similarly distributed between −10 and 10, yet it shows a higher FDD outside this range compared to the RF method and a lower frequency near zero, suggesting a slightly inferior predictive effect. In contrast, the SVM and Kriging methods display more dispersed FDDs. Although the Kriging method's differences are more concentrated than the SVM method's, with the majority falling within the −10 to 10 range, its overall predictive performance remains inferior to the RF and RNN methods. The SVM method's difference frequency distribution is obviously scattered, with many values outside the

interval of −10 to 10, indicating a relatively poor predictive effect on the large-scale dataset among the four methods.

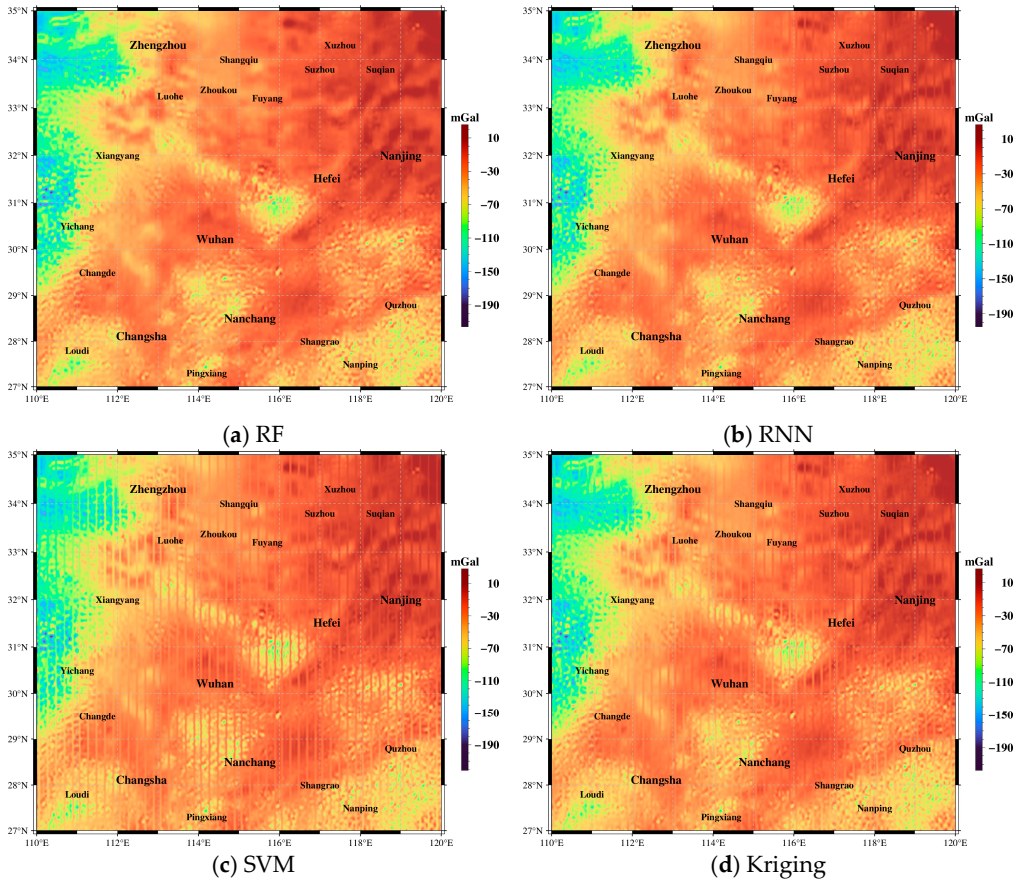


Figure 7. Predicted gravity data for the large-scale dataset; (**a**–**d**) the predicted values for RF, RNN, SVM, and Kriging methods, respectively.

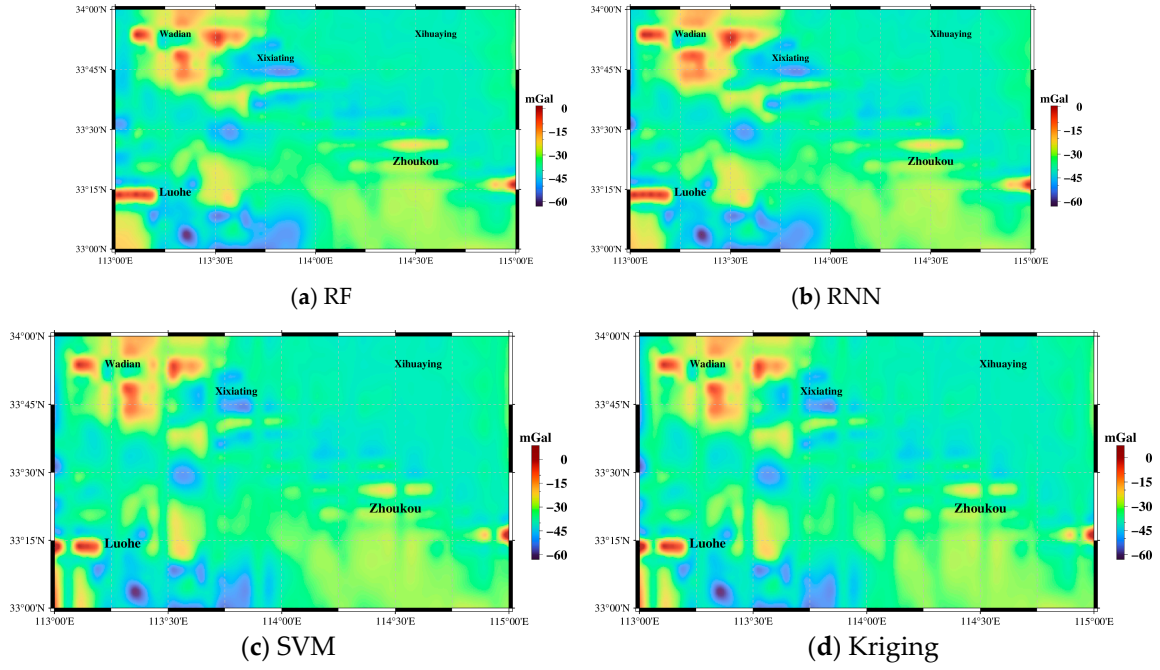


Figure 8. Predicted gravity data for the small-scale dataset; (**a**–**d**) the predicted values for RF, RNN, SVM, and Kriging methods, respectively.

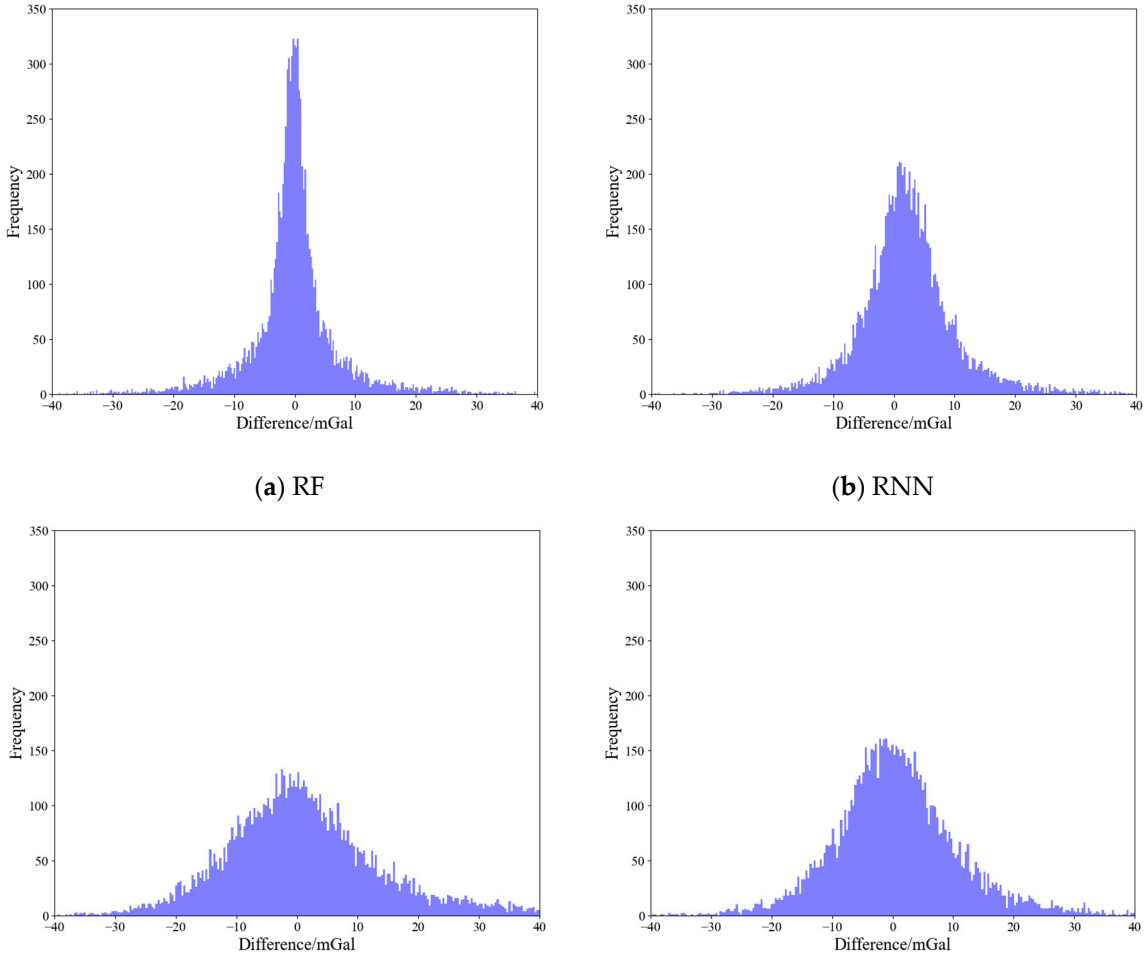
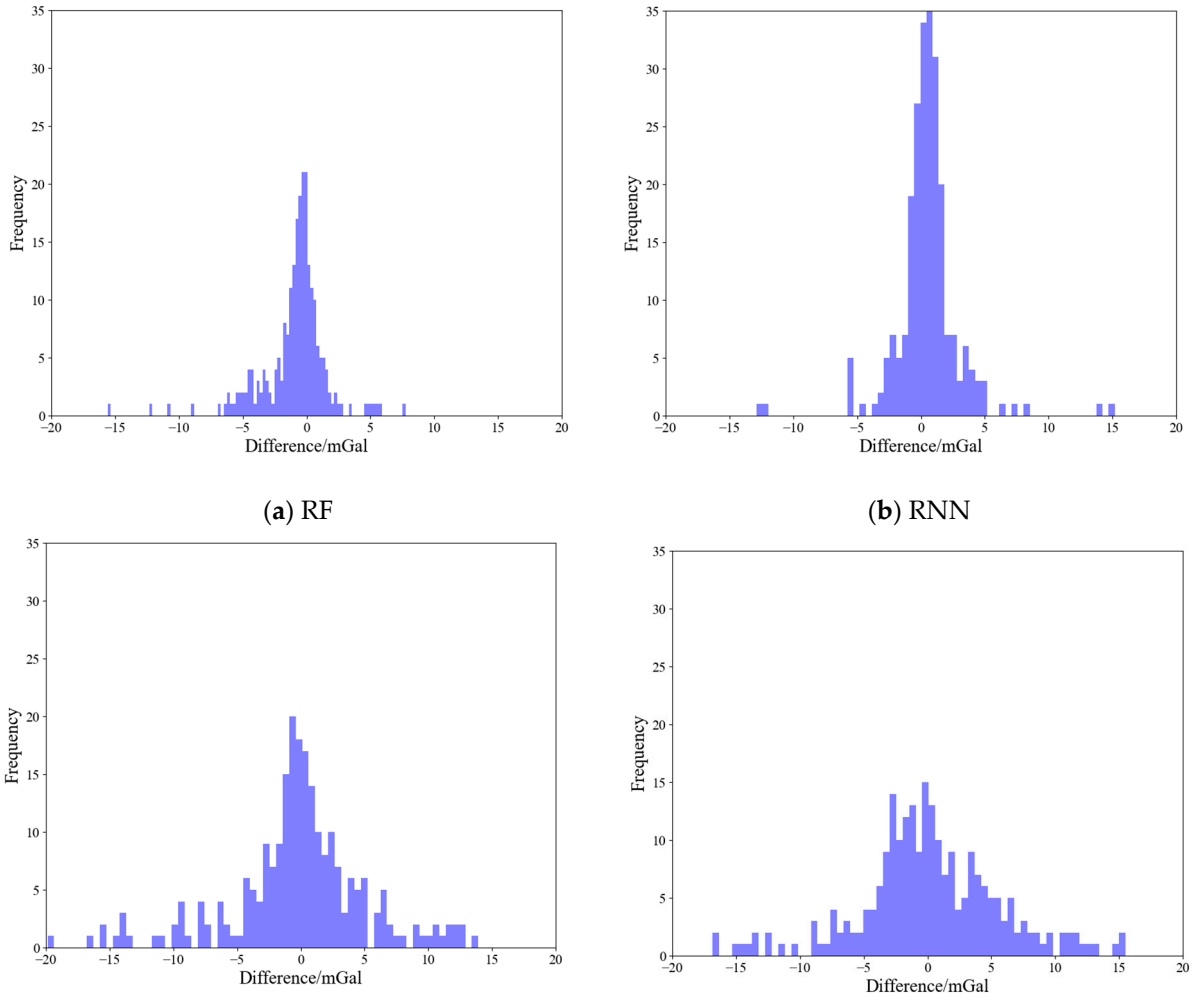


Figure 9. FDD of four methods for the large-scale dataset. The horizontal axis represents the difference, and the vertical axis represents frequency. (**a**–**d**) The RNN, RF, SVM, and Kriging methods, respectively.

Analysis of the difference between predicted and true values for the small-scale dataset, as displayed in Figure 10, reveals that the RNN method's prediction errors are mainly concentrated between −5 and 5, with a higher difference within this range. Obviously, the differences near zero exhibit the highest frequency, indicating superior prediction accuracy for the RNN method. Meanwhile, the RF method also shows a concentration of differences between −5 and 5, but it has a slightly lower frequency near zero compared to the RNN method. Nevertheless, the RF method's predictive performance remains commendable, with fewer differences exceeding this interval, suggesting better prediction stability. On the contrary, the SVM and Kriging methods exhibit more dispersed FDDs, but the SVM's differences are more concentrated within the −5 to 5 range than the Kriging method's, indicating a relatively better predictive effect. However, among the four methods, the Kriging method displays the most dispersed distribution of prediction differences, particularly outside the −5 to 5 range, indicating the lowest predictive effectiveness.

Comparative analysis of the FDD for the large- and small-scale datasets indicates that the RF method maintains relatively stable predictive performance across different dataset sizes. Conversely, the RNN method exhibits a decline in predictive performance when applied to the large-scale dataset. The Kriging method demonstrates poor predictive performance on the small-scale dataset but shows improvement with increased dataset size. Similarly, the SVM method's predictive effectiveness declines on the large-scale dataset. In summary, both the RF and RNN methods display superior prediction effects for both

the large- and small-scale datasets, whereas the SVM and Kriging methods exhibit inferior predictive capabilities.



(**a**) RF (**b**) RNN

(**c**) SVM (**d**) Kriging

Figure 10. FDD of four methods for the small-scale dataset. The horizontal axis represents the difference, and the vertical axis represents frequency. (**a**–**d**) The RNN, RF, SVM, and Kriging methods, respectively.

The predictive results for the large-scale dataset presented in Table 2 reveal that the SVM method exhibits inferior predictive performance, with the highest values for SD, MAE, and RMSE among the four methods at 14.6251 mGal, 10.5137 mGal, and 14.766 mGal, respectively, which suggests that the SVM method's accuracy is lower when processing the large-scale dataset. In comparison, the Kriging method demonstrates improved performance over the SVM method. The RF method, however, excels with the lowest SD, MAE, and RMSE values, indicating superior predictive accuracy. Additionally, the RNN method delivers acceptable predictive results, only slightly higher than those of the RF method. Finally, the RF and RNN methods outperform the others in large-scale dataset predictions, while the SVM method's performance is the poorest, and the Kriging method offers a moderate predictive effect, slightly surpassing the SVM method.

The predictive results of four methods on a small-scale dataset are also presented in Table 2. Consistent with the findings from the large-scale dataset, the machine learning approaches exhibit superior accuracy. The RF method outperforms the others, with the lowest values across all key statistical factors, signifying its superior predictive performance. The RNN method also shows acceptable predictive capabilities, with an MAE close to that of the RF method and only slightly higher RMSE and SD. This suggests that RNN can offer

enhanced accuracy in large-scale dataset predictions. However, the SVM method displays relatively poorer performance, with the highest SD, MAE, and RMSE among the machine learning methods. The poorest-performing method is the Kriging, with the highest SD, MAE, and RMSE values at 6.4474 mGal, 4.3976 mGal, and 6.4522 mGal, respectively.

Table 2. Performance of different methods.

Dataset	Method	SD/mGal	MAE/mGal	RMSE/mGal
Large-scale	RF	2.5773	1.7297	2.7438
	RNN	3.4181	1.7786	3.4804
	SVM	6.3687	4.0431	6.3962
	Kriging	6.4474	4.3976	6.4522
Small-scale	RF	7.6021	4.6187	7.6032
	RNN	8.3971	6.009	8.6699
	SVM	14.6251	10.5137	14.766
	Kriging	10.8593	7.8764	10.8888

3.4. Random Selection Experiment

The random selection experiment mirrors the fixed selection experiment in methodology. Because of the limited experiment data presented in this paper, for the large-scale dataset, there are 192 data points at the same longitudes and 240 data points at the same latitudes. Similarly, for the small-scale dataset, there are 24 data points at the same longitudes and 48 data points at the same latitudes. Therefore, the data trends will recur when the sample reaches a certain number. A total of 250 data points were selected from the large-scale dataset in this paper to more clearly observe data trends; selecting too many data points could lead to repetition, while selecting too few would not allow for a comprehensive observation of the data trends. Similarly, because of the significant fluctuations in the small-scale dataset, 500 data points were selected to adequately observe the data trends. Figure 11 illustrates the prediction accuracy at the 100th data point, which marks a midpoint of a smooth data transition. This transition point allows for a more objective assessment of each method's predictive performance. At this point, the RF method's predictive values closely align with the trend of the true values, indicating superior performance, whereas the RNN, SVM, and Kriging methods exhibit similar prediction curves that do not closely match the true value curve. Meanwhile, the RNN method shows a relatively smaller discrepancy, offering a slightly better predictive effect than the SVM and Kriging methods. However, the predictive effects of the SVM and Kriging methods are poorer, with a significant gap from the true values.

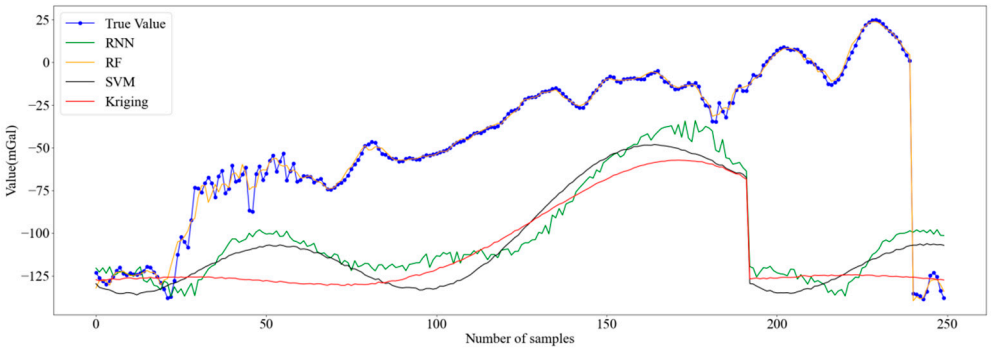


Figure 11. Predicted and true values of the four methods for the large-scale dataset. The blue curve is the true gravity value, and the green, orange, black, and red curves are predicted values for the RNN, RF, SVM, and Kriging methods, respectively. The horizontal axis is the number of samples, and the vertical axis is the predicted values.

Similar to the fixed selection experiment, the 109th data point from the small-scale dataset presented in Figure 12 is selected for analysis. This data point, selected for its

obvious variation in value relative to its adjacent points, serves as a critical benchmark for evaluating the predictive efficacy of different methods. The differences between the predicted and true values for the RF, RNN, SVM, and Kriging methods at this point are 2.55 mGal, 6.48 mGal, 15.69 mGal, and 17.25 mGal, respectively. Observing the overall trend of the predicted values from these four methods reveals that the RF and RNN methods exhibit curve trends closely consistent with the true value trend, indicating superior predictive performance. In contrast, the SVM and Kriging methods demonstrate larger deviations from the true values. Their curves show less fluctuation than those of the RF and RNN methods, indicating an inability to closely match the true values curve, which leads to inferior predictive performance.

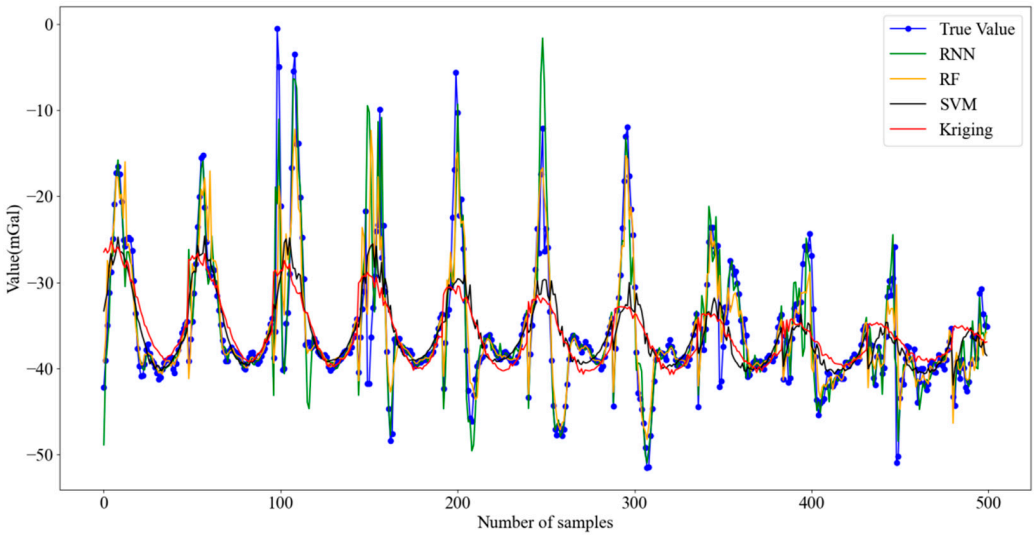


Figure 12. Predicted and true values of the four methods for the small-scale dataset. The blue curve is the true gravity value, and the green, orange, black, and red curves are predicted values for the RNN, RF, SVM, and Kriging methods, respectively. The horizontal axis is the number of samples, and the vertical axis is the predicted values.

A comparison between Figures 11 and 12 reveals that the RF method not only performs well with the large-scale dataset but also retains its superior predictive performance with the small-scale dataset. Meanwhile, the RNN method exhibits acceptable predictive performance on the small-scale dataset, but its effectiveness diminishes when confronted with the large-scale dataset. Additionally, the predictive results of both the SVM and Kriging methods are less than satisfactory for both the large- and small-scale datasets.

The predicted values of the four methods for both the large- and small-scale datasets are shown in Figures 13 and 14, respectively. It is evident that the RF method's predictive performance on the large-scale dataset closely matches the original data, yielding a good prediction result. The RNN method presents a superior predictive result for the small-scale dataset, sometimes even more closely approximating the original dataset than the RF method in certain regions. However, its predictive performance on the large-scale dataset has been observed to diminish. In the meantime, both the SVM method and the Kriging method exhibit poor predictive effects for both the large- and small-scale datasets, being unable to display the details in the original data.

Figure 15 illustrates the difference between predicted and true values within the large-scale dataset. The RF method's difference is mainly concentrated within the −5 to 5 range. In contrast, the RNN, SVM, and Kriging methods exhibit similar differences, predominantly ranging from −100 to 100, with lower differences near zero compared to the RF method, which indicates a lower precision and higher variability in the predictive outcomes of these methods relative to the RF method.

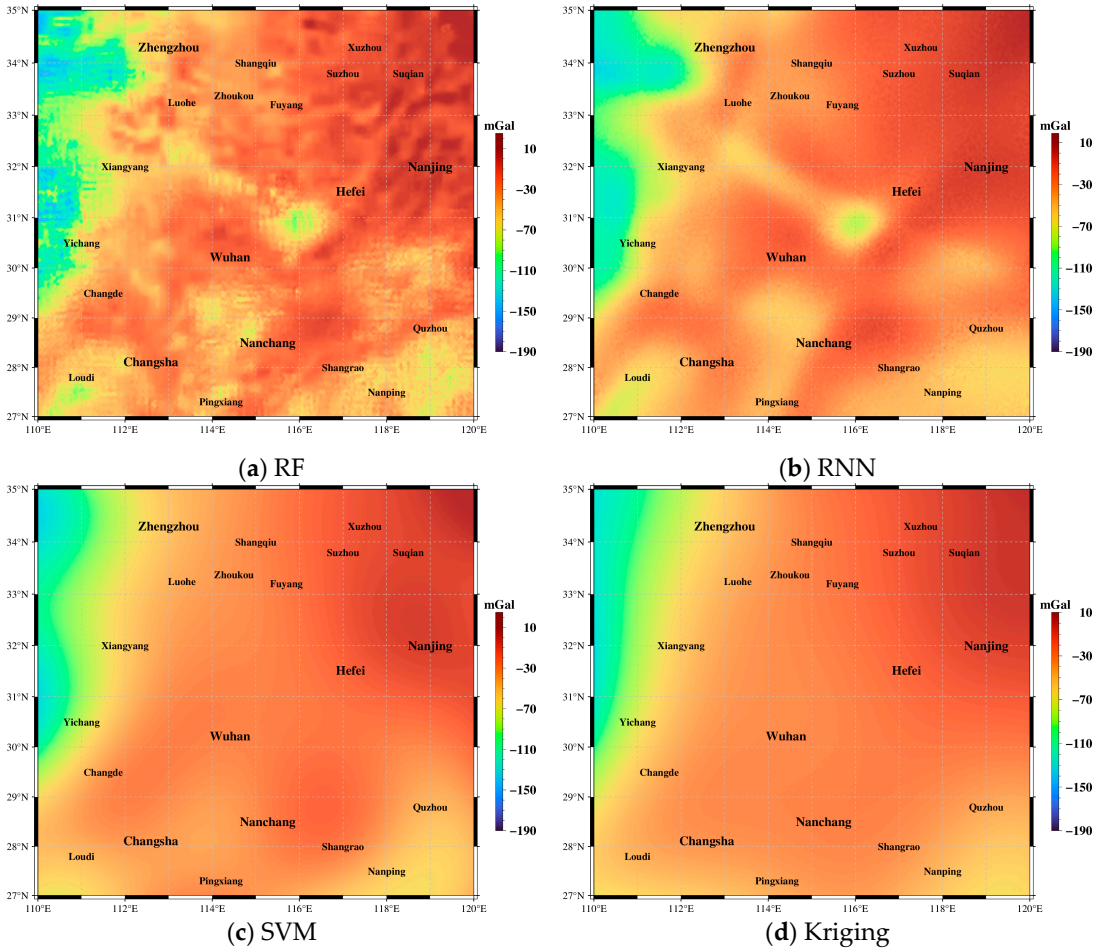


Figure 13. Predicted gravity data for the large-scale dataset. (**a**–**d**) The predicted values for RF, RNN, SVM, and Kriging methods, respectively.

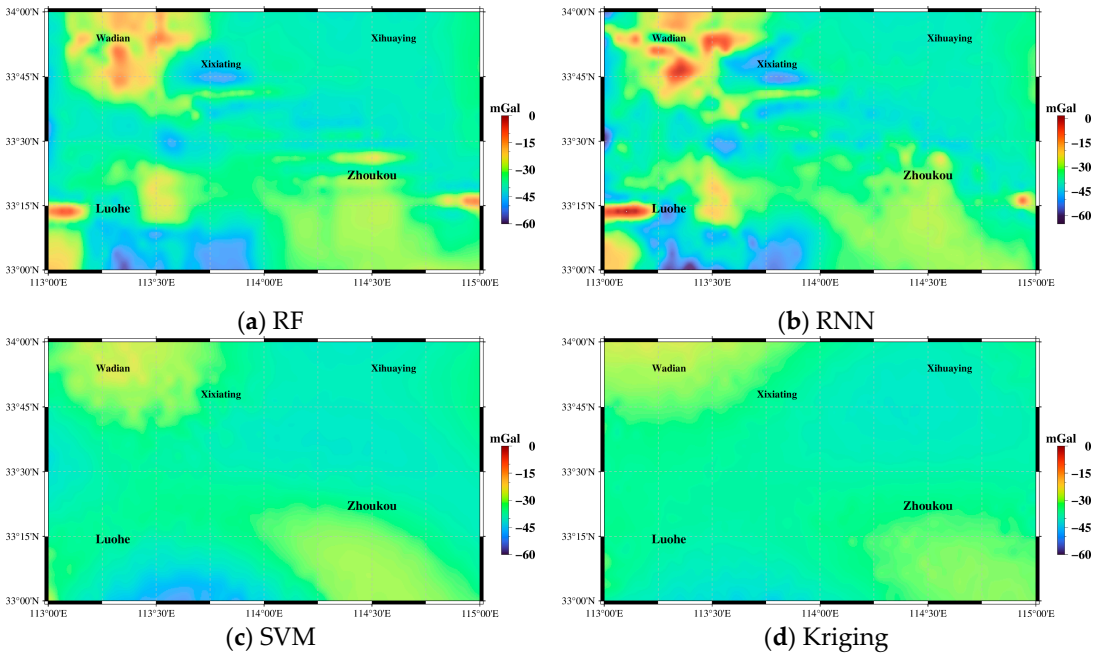


Figure 14. Predicted gravity data for the small-scale dataset. (**a**–**d**) The predicted values for RF, RNN, SVM, and Kriging methods, respectively.

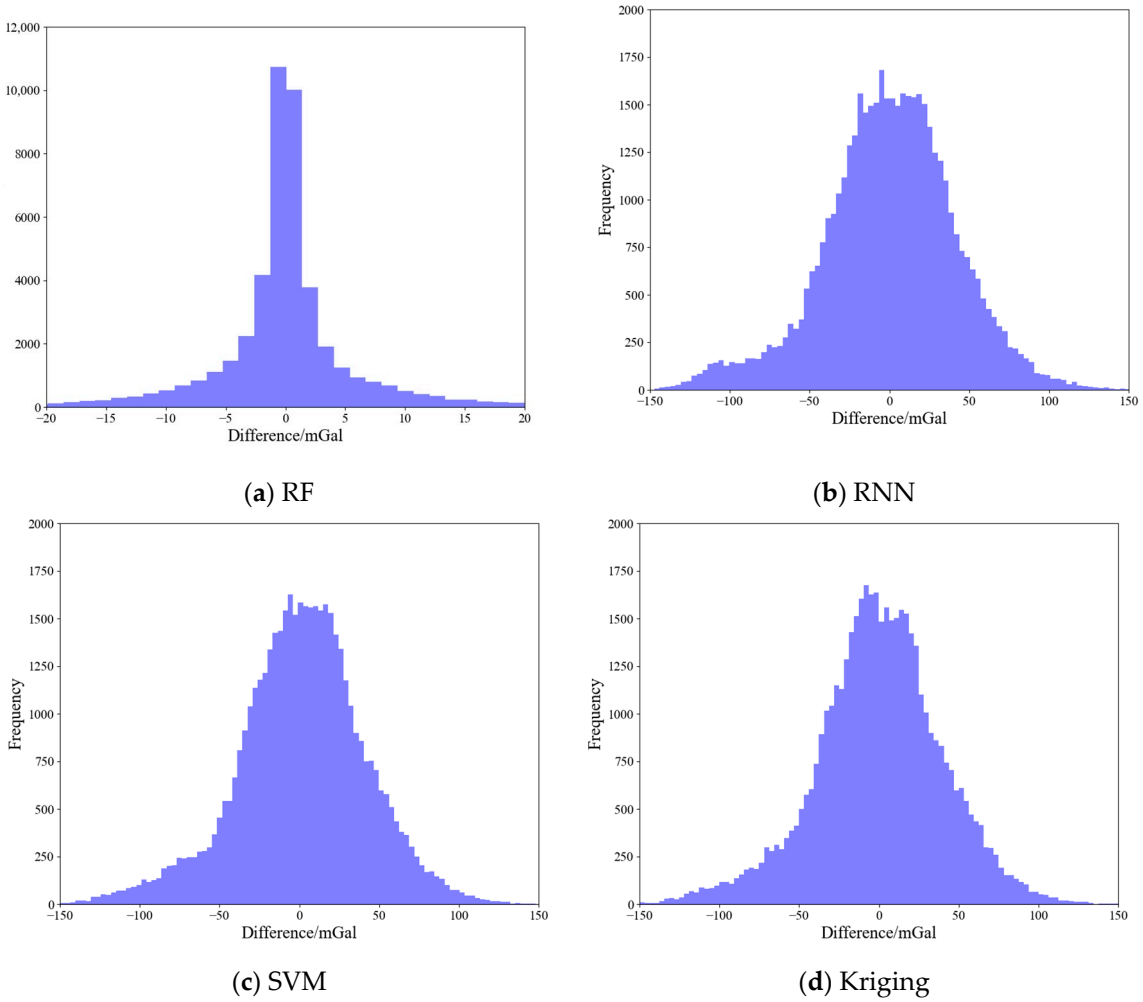


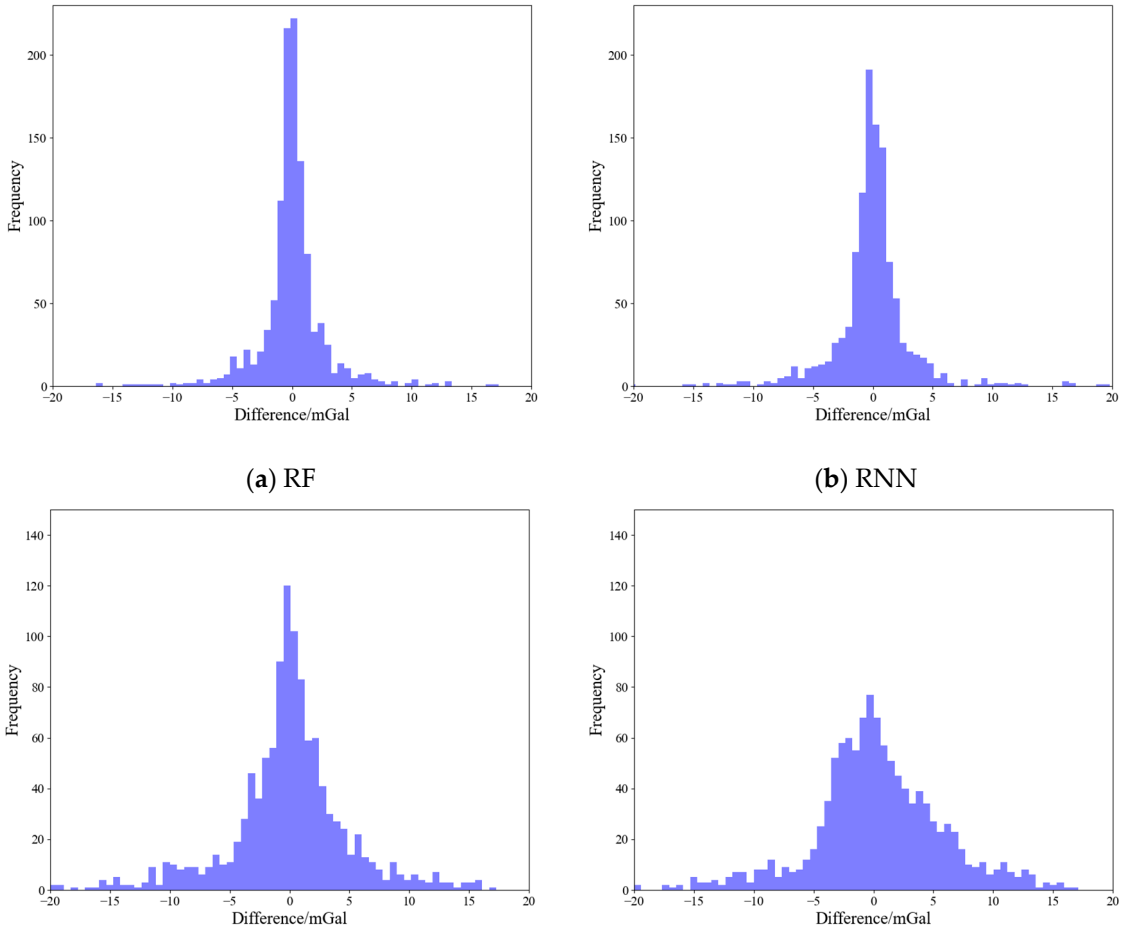
Figure 15. FDD of the four methods for the large-scale dataset. The horizontal axis represents the difference, and the vertical axis represents frequency. (**a**–**d**) The RNN, RF, SVM, and Kriging methods, respectively.

For the small-scale dataset, the FDD of the RF method in Figure 16 is mainly distributed in the range of −5 to 5, peaking in frequency around zero; the RNN method's FDD is also concentrated within the same range, but the frequency near zero is slightly lower than that of the RF method. At the same time, the FDDs of the SVM and Kriging methods are more extensive, with the Kriging method having the most scattered error distribution, especially at high frequencies outside the above interval, indicating its relatively weak predictive performance.

By comparing the FDDs of the large- and small-scale datasets, it can be seen that the RF method is not affected by dataset size and maintains robust prediction performance. However, the predictive performances of the RNN, SVM, and Kriging methods decrease in the large-scale dataset. Overall, the RF method exhibits good predictive ability on both the large- and small-scale datasets; the RNN method shows enhanced proficiency in small dataset scenarios, whereas the SVM and Kriging methods exhibit relatively weaker predictive performances.

According to the predictive results from the large-scale dataset presented in Table 3, the Kriging method exhibits poor predictive performance on the large-scale dataset, with average MAPE, MAE, and RMSE values of 4.0879 mGal, 0.3541 mGal, and 0.4765 mGal, respectively. These values are the highest among the four methods, whereas the R^2 value of 0.7728 is the lowest, indicating a deficiency in predictive accuracy. On the other hand, the RF method performs very well on the large-scale dataset, with the lowest MAPE, MAE,

and RMSE values and the highest R^2 value. The RNN method also delivers satisfactory predictive results. Although its MAPE, MAE, and RMSE values are slightly higher than those of the RF method and its R^2 value is slightly lower, it still offers reliable predictions for the large-scale dataset. In summary, for the prediction of the large-scale dataset, the RF and RNN methods exhibit superior performance, whereas the SVM method performs moderately, slightly outperforming the Kriging method, which is the least effective.



(**a**) RF (**b**) RNN

(**c**) SVM (**d**) Kriging

Figure 16. FDD of the four methods for the small-scale dataset. The horizontal axis represents the difference, and the vertical axis represents frequency. (**a**–**d**) The RNN, RF, SVM, and Kriging methods, respectively.

Table 3. Performance of various methods.

Dataset	Method	MAPE/mGal	MAE/mGal	RMSE/mGal	R^2
Large-scale	RF	1.5031	0.1257	0.2181	0.9524
	RNN	3.0384	0.2240	0.3131	0.9019
	SVM	3.5440	0.3147	0.4405	0.8059
	Kriging	4.0879	0.3541	0.4765	0.7728
Small-scale	RF	2.2389	0.2391	0.4283	0.8018
	RNN	6.2978	0.2635	0.4388	0.7915
	SVM	2.3960	0.4983	0.7932	0.3584
	Kriging	3.8791	0.5872	0.8566	0.2514

Upon further analysis of the predictive performance for the small-scale dataset presented in Table 3, differences in performance variations among the four methodologies—RF, RNN, SVM, and Kriging—are evident. The Kriging method exhibits the poorest performance,

with MAE and RMSE values of 0.5872 mGal and 0.8566 mGal, respectively, which are the highest among the methods. Concurrently, its R^2 value is the lowest, indicating a relatively inferior predictive performance. In comparison, the RF method demonstrates superior performance, highlighting its obvious advantage in predictive accuracy and establishing it as the most distinguished among the four methods. The RNN method also exhibits good prediction results. Its MAE approaches that of the RF method, while its RMSE is slightly higher. Despite a higher MAPE, the RNN's R^2 value is second only to the RF method's, and accurate prediction can still be provided when dealing with the large-scale dataset. The SVM method ranks the lowest among the three machine learning methods in terms of performance; however, it still outperforms the Kriging method, with lower MAE and RMSE values and a higher R^2 value, suggesting that the SVM method's predictive performance is superior to that of the Kriging method.

4. Discussion

Through a detailed comparison of the results of fixed and random selection experiments, it can be seen that the RF method shows good prediction performance for datasets of different sizes under both experimental settings. Regardless of the size of the dataset, the RF method can provide stable and accurate prediction results, which highlights the advantages of RF methods in adapting to different data sizes. Even in the face of significant fluctuations in data sizes, the RF method can still maintain a high level of prediction ability, and its performance is the best among the four methods.

In addition, in the fixed selection experiment, the RNN method also proves its value as an effective prediction method. The RNN method is able to maintain good prediction results on datasets of different sizes. However, in the random selection experiment, the RNN method has better prediction results when dealing with the small-scale dataset, but its performance on the large-scale dataset declines, indicating that although the prediction results of the RNN method are generally good, there are fluctuations in stability. For the SVM method, the performance on the small-scale dataset in fixed selection experiments is acceptable, but the prediction effect on the large-scale-scale dataset drops significantly. In the random selection experiment, the prediction effects of the SVM method on the large- and small-scale datasets are not ideal. As for the Kriging method, the prediction effect is not good on the small-scale dataset with fixed selection experiments, but it is improved on the large-scale dataset, showing that its prediction ability may be improved as the number of data increases. However, in the random selection experiment, the prediction effects of the Kriging method on both the large- and small-scale datasets are unsatisfactory.

In general, the RF method shows high prediction accuracy and stability on datasets of different sizes, while other methods show certain limitations under specific conditions, and the prediction effect is not as good as the RF method.

5. Conclusions

This study presents a comparative analysis of the predictive results between three machine learning methods and the Kriging interpolation method for gravity data. The experimental section is divided into two types of experiments: one featuring a fixed selection of manually selected training and validation datasets and the other employing a random selection through ten-fold cross-validation. The study encompasses datasets of different sizes, with the objective of examining the performance of the four methods under different conditions.

The experimental results reveal that across both the large- and small-scale gravity datasets, the predictive performance of the three machine learning methods consistently surpasses that of the traditional Kriging method. This is evidenced by their lower MAPE, MAE, and RMSE values, alongside higher R^2 values.

Furthermore, within the machine learning methods examined in the experiments, the RF method exhibits the most superior predictive performance, succeeded closely by the RNN method. Both methods demonstrate remarkable predictive capabilities across

datasets of different scales. Conversely, the SVM method ranks the lowest in terms of predictive efficacy among the machine learning methods considered.

From the analysis presented, it is evident that both the RF and the RNN methods exhibit excellent predictive capabilities for different dataset sizes. Their performance consistently outperforms that of traditional Kriging methods. Notably, when processing large-scale data, these methods offer enhanced precision and reliability in their predictive results.

Author Contributions: Conceptualization, Y.L. and Y.Z.; methodology, Y.L.; validation, Q.P. and S.L. (Sulan Liu); formal analysis, Y.Z. and Y.W.; investigation, X.S. and S.L. (Shaobo Li); writing—original draft preparation, Y.L. and Y.Z.; writing—review and editing, Y.W., X.S., S.L. (Shaobo Li) and S.B.; funding acquisition, Y.Z., Y.W. and S.L. (Shaobo Li). All authors have read and agreed to the published version of the manuscript.

Funding: This research was funded by the National Natural Science Fund of China (grant numbers 42274113, 42274111, 41931074, 42304049, 42430101) and the Hubei Provincial Natural Science Foundation of China (grant numbers 2023AFB017).

Data Availability Statement: The EGM2008 gravity model can be downloaded from International Centre for Global Earth Models (ICGEM) (https://icgem.gfz-potsdam.de/tom_longtime, accessed on 1 March 2024.).

Conflicts of Interest: The authors declare no conflicts of interest.

References

1. Sun, W.; Wu, X.P.; Wang, Q.B.; Li, X.X.; Zhu, Z.D. Comparison and analysis of high-precision gravity data gridding methods. *J. Geod. Geodyn.* **2015**, *35*, 342–345. [CrossRef]
2. Zhang, Y.; Yan, J.; Li, F.; Chen, C.; Mei, B.S.; Dohm, J.H. A new bound constraints method for 3-D potential field data inversion using Lagrangian multipliers. *Geophys. J. Int.* **2015**, *201*, 267–275. [CrossRef]
3. Xu, G.; Wu, Y.; Liu, S.; Cheng, S.Y.; Zhang, Y.; Pan, Y.J.; Wang, L.; Dokuchits, E.Y.; Nkwazema, O.C. How 2022 extreme drought influences the spatiotemporal variations of terrestrial water storage in the Yangtze River Catchment: Insights from GRACE-based drought severity index and in-situ measurements. *J. Hydrol.* **2023**, *626*, 130245. [CrossRef]
4. Zhang, Y.; Wu, Y.; Yan, J.; Wang, H.; Rodriguez, J.A.P.; Qiu, Y. 3D inversion of full gravity gradient tensor data in spherical coordinate system using local north-oriented frame. *Earth Planets Space* **2018**, *70*, 58. [CrossRef]
5. Wu, Y.; Liang, F.; Yan, J.; Pei, J.; Zhang, Y. Analysis of regional and residual gravity disturbance of major fault belts in the Tarim Basin, western China. *Remote Sens.* **2022**, *14*, 3948. [CrossRef]
6. Zhang, Y.; Wu, Y.; Chen, C.; Sun, K.; Wang, J. Correlation between gravitational and magnetic anomalies and crustal susceptibility in the Three Gorges area, China. *J. Appl. Geophys.* **2022**, *198*, 104560. [CrossRef]
7. Pang, Q.; Wu, Y.; Chu, R.; Zhang, Y.; Yan, J.; Zhang, L.; Liao, W.; Sun, X.; Dokuchits, E.Y.; Nkwazema, O.C. Deep structural characteristics and dynamic significance of the Southeastern margin of the North China Craton: Insights from gravity/GNSS/seismic observations. *Tectonophysics* **2024**, *874*, 230243. [CrossRef]
8. Hu, D.; Wu, Y.; Xiao, Y.; Qiu, Y.; Wu, X.H.; Zhong, Y.L. Multi-star tracker angular velocity reconstruction method considering temperature effect correction. *Acta Geod. et Cartogr. Sin.* **2024**, *53*, 1748–1760. [CrossRef]
9. Tierra, A.R.; De Freitas, S.R.C. Artificial Neural Network: A Powerful Tool for Predicting Gravity Anomaly from Sparse Data. In Proceedings of the Gravity, Geoid and Space Missions: GGSM 2004 IAG International Symposium, Porto, Portugal, 30 August–3 September 2004.
10. Ren, Q.Q.; Wang, Y.G.; Teng, H.L.; Huang, W.X.; Wang, L. The gravity data forecast of unmeasurable zone based on wavelet neural network. *J. Geod. Geodyn.* **2016**, *36*, 359–363. [CrossRef]
11. She, Y.W.; Fu, G.Y. Estimation of gravity anomaly data based on recurrent neural network. *J. Geod. Geodyn.* **2021**, *41*, 234–237.
12. Liu, Z.; Zhang, Z.; Zhou, C.; Ming, W.; Du, Z. An adaptive inverse-distance weighting interpolation method considering spatial differentiation in 3D geological modeling. *Geosciences* **2021**, *11*, 51. [CrossRef]
13. Amirzehni, P.; Samadianfard, S.; Nazemi, A.H.; Sadraddini, A. Evaluating capabilities of the spline and cubic spline interpolation functions in reference evapotranspiration estimation implementing satellite image data. *Earth Sci. Inform.* **2023**, *16*, 3779–3795. [CrossRef]
14. Malvić, T.; Ivšinović, J.; Velić, J.; Sremac, J.; Barudžija, U. Application of the modified shepard's method (msm): A case study with the interpolation of neogene reservoir variables in northern croatia. *Stats* **2020**, *3*, 68–83. [CrossRef]
15. Losser, T.; Li, L.; Piltner, R. A Spatiotemporal Interpolation Method Using Radial Basis Fnctions for Geospatiotemporal Big Data. In Proceedings of the 2014 Fifth International Conference on Computing for Geospatial Research and Application, Washington, DC, USA, 4–6 August 2014. [CrossRef]

16. Ivšinović, J.; Malvić, T. Application of the radial basis function interpolation method in selected reservoirs of the Croatian part of the Pannonian basin system. *Min. Miner. Depos.* **2020**, *14*, 37–42. [CrossRef]
17. Deng, X.; Tang, Z. Moving surface spline interpolation based on Green's function. *Math. Geosci.* **2011**, *43*, 663–680. [CrossRef]
18. Oliver, M.A.; Webster, R. A tutorial guide to geostatistics: Computing and modelling variograms and kriging. *Catena* **2014**, *113*, 56–69. [CrossRef]
19. Karaca, O.; Erol, B.; Erol, S. Assessments of gravity data gridding using various interpolation approaches for high-resolution geoid computations. *Geosciences* **2024**, *14*, 85. [CrossRef]
20. Xu, Z.; Jiang, Y.; Zhao, L.; Ding, F. Improved shepard method and its application in gravity field data interpolation. *Geomat. Inf. Sci. Wuhan Univ.* **2010**, *35*, 477–480. [CrossRef]
21. Geng, M.X.; Huang, D.N.; Yu, P.; Yang, Q.J. Three-dimensional constrained inversion of full tensor gradiometer data based on cokriging method. *Chin. J. Geophys.* **2016**, *59*, 1849–1860. [CrossRef]
22. Xie, X.H.; Zhao, D.M.; Liu, C.Q. Application of legendre polynomial neural network in gravity data interpolation. *Geomat. Spat. Inf. Technol.* **2023**, *46*, 19–23.
23. Rodriguez-Galiano, V.; Sanchez-Castillo, M.; Chica-Olmo, M.; Chica-Rivas, M.J.O.G.R. Machine learning predictive models for mineral prospectivity: An evaluation of neural networks, random forest, regression trees and support vector machines. *Ore Geol. Rev.* **2015**, *71*, 804–818. [CrossRef]
24. Lou, R.; Lv, Z.; Dang, S.; Su, T.; Li, X. Application of machine learning in ocean data. *Multimed. Syst.* **2023**, *29*, 1815–1824. [CrossRef]
25. Pinter, G.; Felde, I.; Mosavi, A.; Ghamisi, P.; Gloaguen, R. COVID-19 pandemic prediction for Hungary; a hybrid machine learning approach. *Mathematics* **2020**, *8*, 890. [CrossRef]
26. Rajendiran, N.; Sebastian, S.; Kumar, L.S. Cloud segmentation, validation of weather data, and precipitation prediction using machine learning algorithms. *Arab. J. Sci. Eng.* **2024**, *49*, 12259–12289. [CrossRef]
27. Yang, Z.X. Research on machine learning algorithms for big data analysis. *Inf. Rec. Mater.* **2023**, *24*, 92–94. [CrossRef]
28. Sun, T.; Chen, F.; Zhong, L.; Liu, W.; Wang, Y. GIS-based mineral prospectivity mappping using machine learning methods: A case study from Tongling ore district, eastern China. *Ore Geol. Rev.* **2019**, *109*, 26–49. [CrossRef]
29. Chanda, S.; Raghucharan, M.C.; Reddy, K.K.; Chaudhari, V.; Somala, S.N. Duration prediction of Chilean strong motion data using machine learning. *J. S. Am. Earth Sci.* **2021**, *109*, 103253. [CrossRef]
30. Zhang, Z.H.; Liao, X.L.; Cao, Y.Y.; Hou, Z.L.; Fan, X.T. Joint gravity and gravity inversion based on deep learning. *Chin. J. Geophys.* **2021**, *64*, 1435–1452. [CrossRef]
31. Zhang, Z.H.; Yao, Y.; Shi, Z.Y.; Wang, H.; Qiao, Z.K. Deep learning for potential field edge detection. *Chin. J. Geophys.* **2022**, *65*, 1785–1801. [CrossRef]
32. Maiti, S.; Chiluvuru, R.K. A deep CNN-LSTM model for predicting interface depth from gravity data over thrust and fold belts of North East India. *J. Asian Earth Sci.* **2024**, *259*, 105881. [CrossRef]
33. Nourani, V.; Paknezhad, N.J.; Ag, A.; Wen, Z.; Dabrowska, D.; Üzelaltınbulat, S. Application of the machine learning methods for GRACE data based groundwater modeling, a systematic review. *Groundw. Sustain. Dev.* **2024**, *25*, 101113. [CrossRef]
34. Al-Abadi, A.M.; Hassan, A.A.; Al-Moosawi, N.M.; Handhal, A.M.; Alzahrani, H.; Jabbar, F.K.; Anderson, N.L. Drought susceptibility mapping in Iraq using GRACE/GRACE-FO, GLDAS, and machine learning algorithms. *Phys. Chem. Earth* **2024**, *134*, 103583. [CrossRef]
35. Sekulić, A.; Kilibarda, M.; Heuvelink, G.B.M.; Nikolić, M.; Bajat, B. Random forest spatial interpolation. *Remote Sens.* **2020**, *12*, 1687. [CrossRef]
36. Xu, Z.; Leung, J.Y. A novel equation of RNN-based neural network with real-time updating–An application for dynamic hydraulic fractured shale gas production forecasting. *Geoenergy Sci. Eng.* **2024**, *233*, 212491. [CrossRef]
37. Sahoo, A.; Samantaray, S.; Ghose, D.K. Multilayer perceptron and support vector machine trained with grey wolf optimizer for predicting floods in barak river, India. *J. Earth Syst. Sci.* **2022**, *131*, 85. [CrossRef]
38. Wang, F.; Xuan, Z.; Zhen, Z.; Li, K.; Wang, T.; Shi, M. A day-ahead PV power forecasting method based on LSTM-RNN model and time correlation modification under partial daily pattern prediction framework. *Energy Convers. Manag.* **2020**, *212*, 112766. [CrossRef]
39. Yang, L.; Wu, Y.X.; Wang, J.L.; Liu, Y.L. Research on recurrent neural network. *J. Comput. Appl.* **2018**, *38*, 1–6. [CrossRef]
40. Mou, L.; Ghamisi, P.; Zhu, X.X. Deep recurrent neural networks for hyperspectral image classification. *IEEE Trans. Geosci. Remote Sens.* **2017**, *55*, 3639–3655. [CrossRef]
41. Zhang, X.Y.; Yin, F.; Zhang, Y.M.; Liu, C.L.; Bengio, Y. Drawing and recognizing Chinese characters with recurrent neural network. *IEEE Trans. Pattern Anal. Mach. Intell.* **2018**, *40*, 849–862. [CrossRef]
42. Del Río, S.; López, V.; Benítez, J.M.; Herrera, F. On the use of map reduce for imbalanced big data using random forest. *Inf. Sci.* **2014**, *285*, 112–137. [CrossRef]
43. Belgiu, M.; Drăguţ, L. Random forest in remote sensing: A review of applications and future directions. *ISPRS J. Photogramm. Remote Sens.* **2016**, *114*, 24–31. [CrossRef]
44. Sarkar, H.; Goriwale, S.S.; Ghosh, J.K.; Ojha, C.S.P.; Ghosh, S.K. Potential of machine learning algorithms in groundwater level prediction using temporal gravity data. *Groundw. Sustain. Dev.* **2024**, *25*, 101114. [CrossRef]
45. Noble, W.S. What is a support vector machine? *Nat. Biotechnol.* **2006**, *24*, 1565–1567. [CrossRef] [PubMed]

46. Huang, Y.; Zhao, L. Review on landslide susceptibility mapping using support vector machines. *Catena* **2018**, *165*, 520–529. [CrossRef]
47. Huang, S.; Cai, N.; Pacheco, P.P.; Narrandes, S.; Wang, Y.; Xu, W. Applications of support vector machine (SVM) learning in cancer genomics. *Cancer Genom. Proteom.* **2018**, *15*, 41–51. [CrossRef]
48. Natarajan, N.; Sudheer, C. Groundwater level forecasting using soft computing techniques. *Neural Comput. Appl.* **2020**, *32*, 7691–7708. [CrossRef]
49. Zhou, Y.Y.; Zhang, H.G.; Hu, X.J. Improved kriging interpolation based on support vector machine: A case study on the PM_(2.5) data of fenwei plain. *Sci. Technol. Eng.* **2023**, *23*, 10575–10584.
50. Jin, G.D.; Liu, Y.C.; Niu, W.J. Comparison between inverse distance weighting method and kriging. *J. Chanchun Univ. Technol.* **2003**, *24*, 53–57. [CrossRef]
51. Li, Z.H.; Fang, Y.F. Research of gravity data's interpolation by ordinary kriging method. *J. Gromatics Feb* **2010**, *35*, 42–43. [CrossRef]
52. Min, K.; Ni, F.; Chen, Z.; Liu, H.; Lee, C.H. A robot positional error compensation method based on improved kriging interpolation and Kronecker products. *IEEE Trans. Ind. Electron.* **2023**, *71*, 3884–3893. [CrossRef]
53. Pavlis, N.K.; Holmes, S.A.; Kenyon, S.C.; Factor, J.K. The development and evaluation of the earth gravitational model 2008 (EGM2008). *J. Geophys. Res. Solid Earth* **2012**, *117*, B04406. [CrossRef]
54. Chai, T.; Draxler, R.R. Root mean square error (RMSE) or mean absolute error (MAE)?–arguments against avoiding RMSE in the literature. *Geosci. Model Dev.* **2014**, *7*, 1247–1250. [CrossRef]

Disclaimer/Publisher's Note: The statements, opinions and data contained in all publications are solely those of the individual author(s) and contributor(s) and not of MDPI and/or the editor(s). MDPI and/or the editor(s) disclaim responsibility for any injury to people or property resulting from any ideas, methods, instructions or products referred to in the content.